Conjugated microporous polymers containing ferrocene units for high carbon dioxide uptake and energy storage

Maha Mohamed Samy [a,b,1], Santosh U. Sharma [c,1], Mohamed Gamal Mohamed [a,b,**], Ahmed A.K. Mohammed [b], Swetha V. Chaganti [c], Jyh-Tsung Lee [c,d], Shiao-Wei Kuo [a,d,*]

[a] Department of Materials and Optoelectronic Science, Center of Crystal Research, National Sun Yat-Sen University, Kaohsiung, 804, Taiwan
[b] Chemistry Department, Faculty of Science, Assiut University, Assiut, Egypt
[c] Department of Chemistry, National Sun Yat-Sen University, Kaohsiung, 80424, Taiwan
[d] Department of Medicinal and Applied Chemistry, Kaohsiung Medical University, Kaohsiung, 807, Taiwan

H I G H L I G H T S

- Conjugated microporous polymers containing ferrocene moieties were successfully constructed.
- Our AFC-CMPs possessed outstanding thermal stability and suitable surface areas.
- The amounts of CO_2 adsorbed by BP-FC-CMP were 1.3 and 2.22 mmol g^{-1} at 298 and 273 K: respectively.
- The BP-FC-CMP electrode achieved the highest specific capacitance and capacity retention.

A R T I C L E   I N F O

A B S T R A C T

In this study, we employed facile aminative cyclizations (Chichibabin pyridine reactions) of 1,1′-diacetylferrocene (AFC) with aryl aldehydes to prepare conjugated microporous polymers (CMPs) containing ferrocene moieties, for supercapacitor applications. The chemical structure of these AFC-CMPs frameworks was proved by using FTIR and solid ^{13}C NMR spectroscopies. All these AFC-CMPs featured outstanding thermal stability with decomposition temperature (T_{d10}) ranging from 309 to 337 °C and also these AFC-CMPs possess an amorphous structure with BET values in the range 72–341 m^2 g^{-1}. Among our tested systems, the BP-FC-CMP electrode achieved the highest specific capacitance of 608 F g^{-1} at a 0.5 A g^{-1} and the highest capacity retention of 97.47% after 2000 cycles and good CO_2 ability uptake. This behavior arose from its high porosity facilitating redox reactions with faster kinetics. These novel metal-free CMPs have promise for application in secondary energy devices.

1. Introduction

Demand for greenhouse gas-free energy has led to the emergence of various energy harvesting techniques. Nevertheless, total reliance on renewable sources of energy will not be sufficient for meeting daily energy requirements; we will have to find systematic and cost-effective ways of storing and harvesting energy. Supercapacitors (SCs) have attracted much attention among the many available electrochemical energy storage (EES) systems because of high energy densities (in comparison with dielectric capacitors), high power densities, and long-life performance (durability). These attractive characteristics also make SCs useful in various other devices, including wind turbines, hybrid buses/trams, and biomedical defibrillators [1–8]. Many factors contribute to the electrical charge storing ability of SCs: (i) physical charge separation across the interfaces of EDLCs, commonly employing porous carbons as electrodes; (ii) Faradaic reactions between

* Corresponding author. Department of Materials and Optoelectronic Science, Center of Crystal Research, National Sun Yat-Sen University, Kaohsiung, 804, Taiwan.
** Corresponding author. Department of Materials and Optoelectronic Science, Center of Crystal Research, National Sun Yat-Sen University, Kaohsiung, 804, Taiwan.
E-mail addresses: mgamal.eldin12@yahoo.com (M.G. Mohamed), kuosw@faculty.nsysu.edu.tw (S.-W. Kuo).
[1] These authors contributed equally to this work.
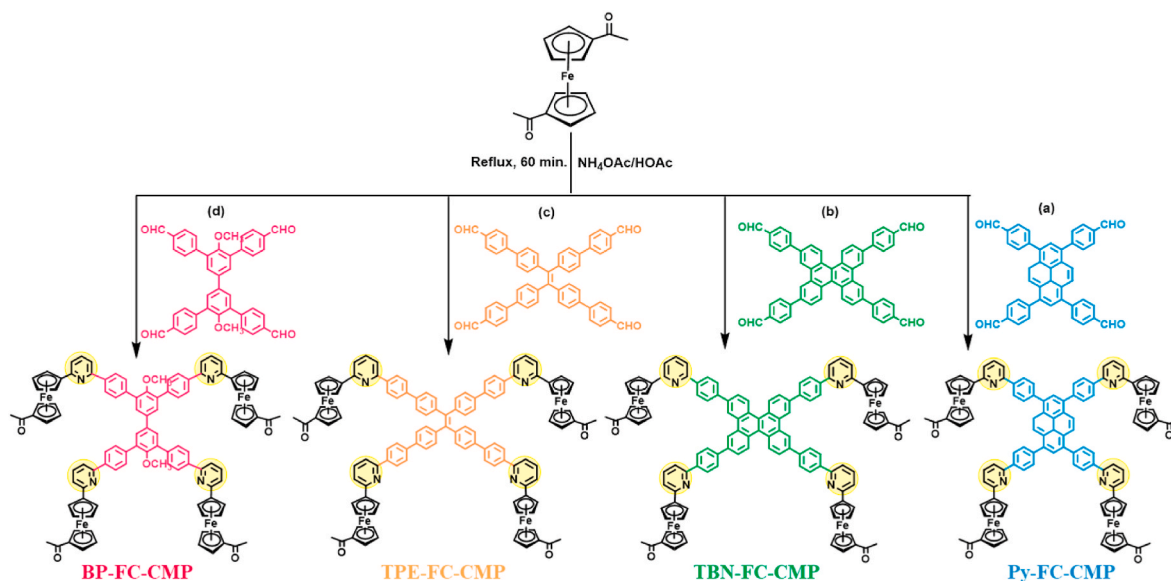
Scheme 1. Synthesis of (a) Py-FC, (b) TBN-FC, (c) TPE-FC, and (d) BP-FC-CMPs.

electrolytes and redox-active organic moieties (e.g., conjugated polymers); and (iii) reactions occurring at the surfaces of the electrode materials [9–12]. Thus, the type and composition of the electrode material play critical roles affecting the performance of SCs [13–16]. The electrode materials usually comprise different kinds of compounds, including sulfides, hydroxides, metal oxides and porous carbonaceous precursors. Because of the versatility, availability of raw materials, high sustainability, and environmental friendliness of organic electroactive materials, they are potential alternatives to toxic inorganic compounds for use as electrode materials for SCs [14,17–21].In general, the surface of the electrode undergoes electrochemical reactions, while its pores are responsible for ion mitigation.

Porous materials are classified according to pore size into three types including microporous, mesoporous, and macroporous: respectively [22,23]. Microporous organic polymers (MOPs) have gained attention from industry and academia as next-generation materials that are easy to prepare with very high physical surface areas, good thermal stabilities, low densities, high pore volumes, and large Brunauer–Emmett–-Teller (BET) surface areas. Accordingly, MOPs appear useful for application in, for example, CO_2 reduction, gas separation and storage, heterogeneous catalysis, oil scavenging, hydrogen evolution, and water treatment. MOPs have been prepared in various porous forms such as conjugated microporous polymers (CMPs), intrinsically microporous polymers (PIMs), and porous aromatic frameworks (PAFs) all of which encourage various network-type activities [16]. COFs and some CTFs are usually crystalline and formed under thermodynamic conditions, while the other types of MOPs are usually amorphous. Despite their different topological characteristics, MOPs are light-weight, strongly covalently bonded, porous, and have 2D or 3D compounds [4,24–33]. In particular, CMPs are highly flexible porous polymers, stable nanopores, and expanded π-conjugation. CMPs have been synthesized through oxidative polymerization and conventional coupling reactions [10,34–36]. CMPs are easy to prepare and have large surface areas, porosities, strong visible light activities, high thermal stabilities, and superb optoelectronic capabilities [37–51]. Due to their wide range of potential building blocks, ready structural tunability, and diversity of π-conjugated units, CMPs are more useful than other standard electrode materials when designing electrode materials for high-performance SCs [52,53].

Ferrocene is a frequent component in organometallic systems that has aroused a lot of interest in the area of organometallic chemistry due to its redox ability and stable sandwich structure. Because the incorporation of a ferrocenyl unit into a polymer skeleton opens up new possibilities for magnetic switches, enantioselective catalysis, and redox batteries [54–61]. The addition of a ferrocenyl unit to the molecules is expected to provide the properties of the materials including reversible ferrocene/ferrocenium couplings, planar chirality, and stable iron sources. As a result, in these fields of study, unique molecular approaches for endeavor applications are essential. The usage of ferrocene-based polymers, which have seen rapid expansion in applications ranging from redox batteries to precursor-derived ceramics, is one of the most powerful approaches [56–62]. For example, Wang et al. fabricated a FcTz-POP by incorporating Fc units as building blocks through Schiff base reactions; iodine capture by the FcTz-POP (396 wt% at 348 K) was 1.8 times higher than that of a corresponding ferrocene-free BpTz-POP material [63]. Ma and co-workers designed Fc-based CMPs containing Fc linkages in their backbones and studied their use in the adsorption and photocatalytic decomposition of contaminants under visible light; their Fc-TEB-CMP displayed excellent performance for the degradation of methylene blue (reaching 99%) under visible light, superior to that of commercial TiO_2, and also the ability to convert 2-chloroethyl ethyl sulfide into nontoxic materials [64]. Moreover, Tan et al. synthesized two conjugated microporous polymers (FcCMP-1 and FcCMP-2) from 1,1′-dibromoferrocene through Yamamoto coupling and found that they could were efficient adsorbents for dye removal [65]. In addition, Wei and co-workers prepared hyperbranched polymers based on ferrocene units in the form of spheres and hollow polyhedral for the removal of pollutants from water and lithium batteries [66].

In this study, a series of redox-active ferrocene-based CMPs (AFC-CMPs) have been prepared for applying as electrode materials in supercapacitors. We synthesized them through aminative cyclizations (Chichibabin pyridine reactions) of 1,1′-diacetylferrocene (AFC) with four different aryl aldehydes [1,3,6,8-tetra(4-formylphenyl)pyrene (Py-CHO), 2,7,10,15-tetra(4-formylphenyl)tetrabenzonaphthalene (TBN-CHO), 1,1,2,2-tetrakis(4-formyl-(1,1′-biphenyl))ethane (TPE-CHO), and 3,3′,5,5′-tetra (4-formylphenyl)-4,4′-dimethoxybiphenyl (BP–CHO) in acetic acid, without adding any catalysts (Scheme 1). These AFC-CMPs possessed redox-active Fc units that could undergo rapid reversible reactions, contributing to enhanced pseudocapacitance, and allowing the efficient movement of the electrolyte through the pores of the CMP, contributing to enhanced efficiency [67].
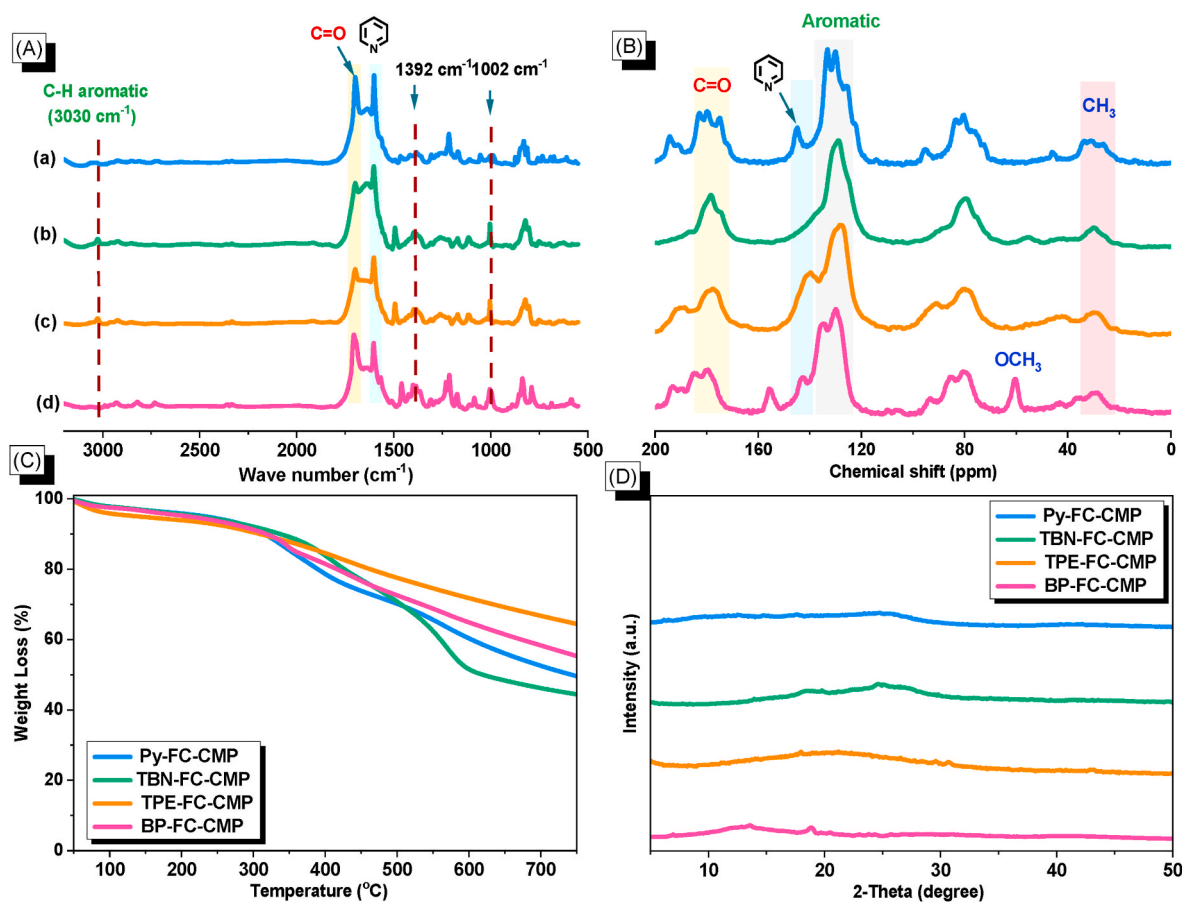
Fig. 1. (A) FTIR, (B) solid ^{13}C NMR, (C) TGA, and (D) XRD profiles of Py-FC, TBN-FC, TPE-FC, and BP-FC-CMPs.

2. Experimental

2.1. Materials

Ferrocene, 4-formylphenylboronic, Pd(PPh$_3$)$_4$, anhydrous AlCl$_3$, acetyl chloride (AcCl), ammonium acetate (NH$_4$OAc), K$_2$CO$_3$, dichloromethane (CH$_2$Cl$_2$), 1,4-dioxane, acetic acid (AcOH), and hydrochloric acid (HCl) were received from various trade sources (Sigma–Aldrich, Acros, Alfa Aesar) and used directly as obtained. The preparation of 3,3′,5,5′-tetrabromo-4,4′-biphenol (BP–4Br-OH), 3,3′,5,5′-tetrabromo-4,4′-dimethoxy-1,1′-biphenyl (BP–4Br–OCH$_3$), and their corresponding data including FTIR, and NMR spectroscopy were found in supporting information [Scheme S3, Figs. S7–S11]. Py-CHO, TPE-CHO, and 2,7,10,15-tetrabromotetrabenzonaphthalene (TBN-Br$_4$) were prepared using methods described previously [30,32,40,41,43,44,47].

2.1.1. 1,1′-Diacetylferrocene (AFC)

Ferrocene (8.06 mmol) in dichloromethane (25 mL) was added to a stirred mixture of acetyl chloride (17.71 mmol) and aluminum chloride (17.71 mmol). Then, the reaction was continued stirring overnight at ambient temperature. After that, the contents of the reaction were poured onto ice cubes-water mixture, filtered, washed severely with water, and dried at 70 °C to afford a dark red solid (Scheme S1). FTIR (Fig. S1): 3089, 1667 (C=O), 1390 and 1010 (C=C stretching of cyclopentadiene rings). ^{1}H NMR (Fig. S2): 4.79 (s, 4H), 4.59 (s, 4H), 2.28 (s, 6H). ^{13}C NMR (Fig. S2): 200.25, 80.37, 73.29, 70.58, 27.21. (+) ESI-MS: *m/z* 270.01 (calcd for C$_{14}$H$_{14}$FeO$_2$) (Fig. S3).

2.1.2. 2,7,10,15-tetra(4-formylphenyl)tetrabenzonaphthalene (TBN-CHO)

TBN-Br$_4$ (0.83 mmol), 4-formylphenylboronic acid (0.83 mmol), Pd (PPh$_3$)$_4$ (0.84 mmol), and K$_2$CO$_3$ (0.832 mmol) were mixed together and degassed using nitrogen pump. Next, *p*-dioxane (40 mL) was put into the contents and kept for heating at 90 °C for 2 days. After that, the reaction contents were added to the ice/cold water mixture followed by neutralization with HCl (3 mL) to dissolve potassium carbonate. The resulted yellow solid was poured into methanol (40 ml) and heated for 30 min to take off any reactants that may be present. Finally, the powder was filtered and dried to produce the TBN-CHO (Scheme S2). FTIR (Fig. S4): 3036 (C–H aromatic), 2825, 2735 (CH=O), 1692 (C=O). ^{1}H NMR (Fig. S5): 10.083 (s, 4H, CH=O), 8.050–7.748 (m, 28H, CH aromatic), ^{13}C NMR (Fig. S6): 192.82, 144.38, 135.80, 135.08, 134.53, 134.53, 130.19, 130.13, 128.28, 127.92, 127.13, 115.84.

2.1.3. 3,3′,5,5′-tetra (4-formylphenyl)-4,4′-dimethoxybiphenyl (BP–CHO)

BP-4Br-OCH$_3$ (1.01 mmol), Pd(PPh$_3$)$_4$ (0.05 mmol), 4-formylphenylboronic acid (6.53 mmol), and K$_2$CO$_3$ (16.64 mmol) were degassed together under vacuum nitrogen pump, then 1,4-dioxane (50 mL) was added and the to the mixture was allowed for heating at 85 °C for two days. After that, the reaction contents were poured onto ice-cold water and neutralized with HCl (2 mL) to dissolve any remained amount of K$_2$CO$_3$. The obtained residue was washed with methanol to produce white powder (Scheme S3). FTIR (Fig. S9): 3067 (CH aromatic), 2988, 2929 (CH aliphatic), 2821, 2733 (CH=O), 1689 (C=O), 1610 (C=C). ^{1}H NMR (Fig. S10): 10.087 (s, 4H, CHO), 8.034–7.901 (m, CH aromatic), 3.130 (s, 6H, OCH$_3$). ^{13}C NMR (Fig. S11): 192.889, 143.831, 135.112, 134.607, 130.086, 129.625, 129.449, 60.713.

Table 1
TGA and BET data of Py–FC–CMP, TBN–FC–CMP, TPE–FC–CMP, and BP-FC-CMP.

Sample	T_{d5} (°C)	T_{d10} (°C)	Char yield (wt%)	Surface area (m^2 g^{-1})	Pore size (nm)
Py–FC–CMP	233	315	47	72	1.82
TBN–FC–CMP	225	337	43	217	0.41–1.54
TPE–FC–CMP	140	309	63	271	0.40–1.78
BP-FC-CMP	210	317	52	341	0.43–1.90

2.2. AFC-CMPs

As a representative example, BP-CHO (0.237 mmol), AFC (0.48 mmol) and ammonium acetate (7.26 mmol) were heated into acetic acid (25 mL) at 120 °C for 12 h. After that, the solid gained was filtered, washed with aqueous ammonia (1%), hot water, THE, MeOH, and acetone, subsequently. Finally, the product, defined as BP-FC-CMP was kept in the oven at 100 °C for drying for at least two days. Comparable to the preparation of BP-FC-CMP, Py-CHO (0.15 g, 0.24 mmol), or TPE-CHO (0.15, 0.20 mmol) or TBN-CHO (0.15, 0.20 mmol) were utilized to produce Py–FC–CMP, TPE–FC–CMP and TBN–FC–CMP, respectively (Scheme 1). FTIR (Fig. 1(a)): 3027, 2924, 1702 (C=O), 1637 (pyridyl ring), 1392 and 1002 cm^{-1} (C=C stretching of cyclopentadiene rings).

3. Results and discussion

3.1. Synthesis of AFC

The AFC monomer building block was achieved through Friedel-Crafts acylation of monomer was obtained through Friedel–Crafts acylation of Fc with AcCl and AlCl$_3$ (molar ratio = 1:2.2:2.2) in CH$_2$Cl$_2$ (Scheme S1). The AFC structure was confirmed by using FT-IR and NMR analyses [Figs. S1–S2]. The FTIR spectrum (Fig. S1) confirmed the acylation of Fc into AFC through the appearance of a strong absorption peak at 1667 cm^{-1} for the C=O group. ^{1}H NMR spectrum [Fig. S2(A)] presented sharp signals at 2.28, 4.59, and 4.79 ppm that related to aliphatic protons of acetyl (CH$_3$–CO) group and cyclopentadienyl protons of ferrocene ring, respectively. For more evidence, ^{13}C NMR profile

[Fig. S2(B)] ascribed signals for acetyl group at 27.21 ppm (CH$_3$) and 200.25 ppm (C=O), and also major signals for carbons of ferrocene moiety were found at 70.58, 73.29, and 80.37 ppm, respectively.

3.2. Synthetic design and structural characterization of AFC-CMPs

The Fc-containing CMPs Py–FC–CMP, TBN–FC–CMP, TPE–FC–CMP, and BP-FC-CMP were obtained through aminative cyclizations of AFC with the aryl aldehydes Py-CHO, TBN-CHO, TPE-CHO, and BP-CHO, respectively, boiling in acetic acid at 120 °C in the presence of NH$_4$OAc, without the need for any metal catalyst (Scheme 1). The structural frameworks of the AFC-CMPs were identified and were proved by using two main characterizations FTIR and solid ^{13}C NMR spectroscopies. The FTIR analysis of the four AFC-CMPs [Fig. 1(a)] displayed signals at 1637 cm^{-1}, representing the formation of pyridine rings in their reticular frameworks, and 1702 cm^{-1}, representing the C=O groups of remaining acetyl units that remained unreacted because of steric bulk. Furthermore, the presence of Fc moieties was characterized by absorption peaks at 1392 and 1002 cm^{-1} for the C=C stretching vibrations of the cyclopentadiene rings. The solid-state ^{13}C NMR [Fig. 1 (b)] of four AFC-CMPs featured signals near 143 ppm and from 127 to 130 ppm representing carbon nuclei in the pyridine and other aromatic rings. The resonances from 80 to 90 ppm were assigned to the Fc units in the AFC-CMPs, in agreement with previously reported results [63]. Three signals near 29, 179, and 190 ppm were present in the spectra of the AFC-CMPs, representing terminal acetyl and aldehyde groups [68]. In addition, the spectrum of BP-FC-CMP featured a peak at 59 ppm representing its methoxy (OCH$_3$) groups. Thus, the above spectra were consistent with the supposed structures of the AFC-CMPs in Scheme 1. Thermogravimetric analysis [Fig. 1(c), Table 1] revealed that the AFC-CMPs derived from Py-CHO, TBN-CHO, TPE-CHO, and BP-CHO had high thermal stabilities up to 300 °C, with 10 wt% decomposition temperatures of 315, 337, 309 and 317 °C, respectively, and residual weights at 800 °C of 47, 43, 63, and 52 wt%, respectively, suggesting the formation of networks with high cross-linking density. Powder X-ray diffraction (PXRD) of all the AFC-CMPs featured comparatively broad diffraction peaks at high diffraction angles (2θ = ca. 25°), confirming their amorphous frameworks [Fig. 1(d)] [63]. We used X-ray
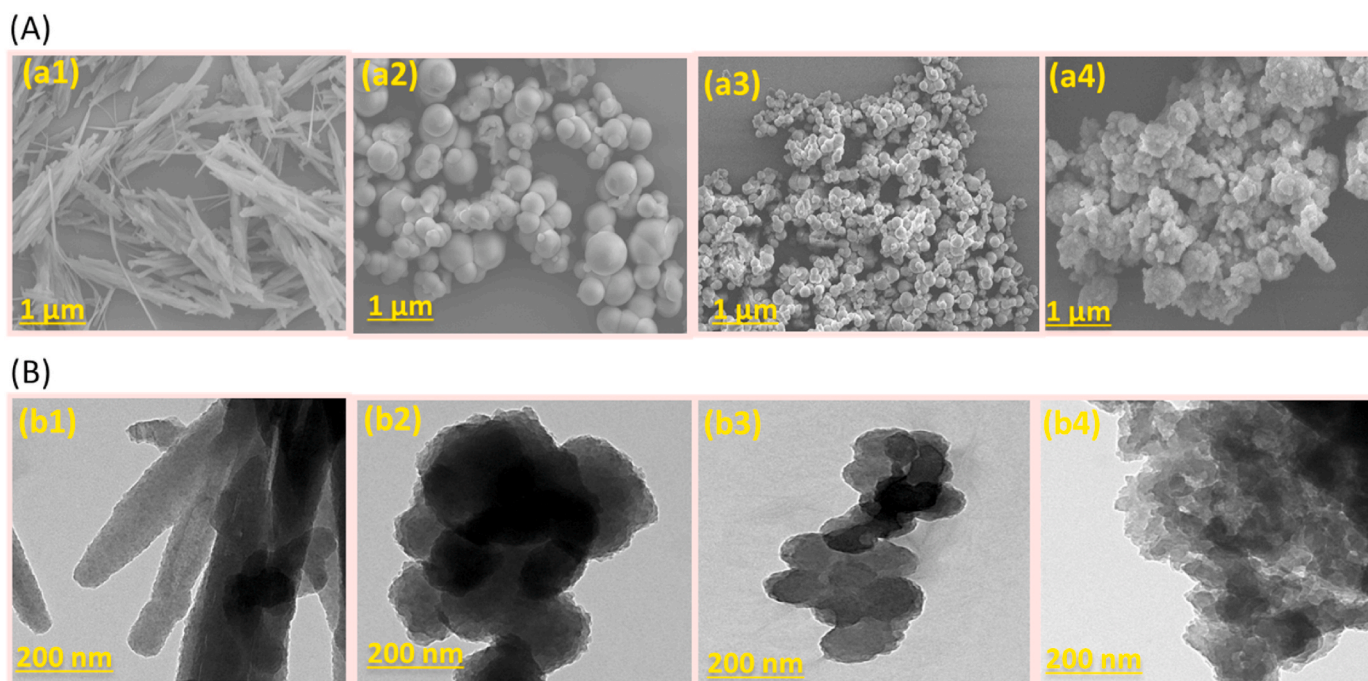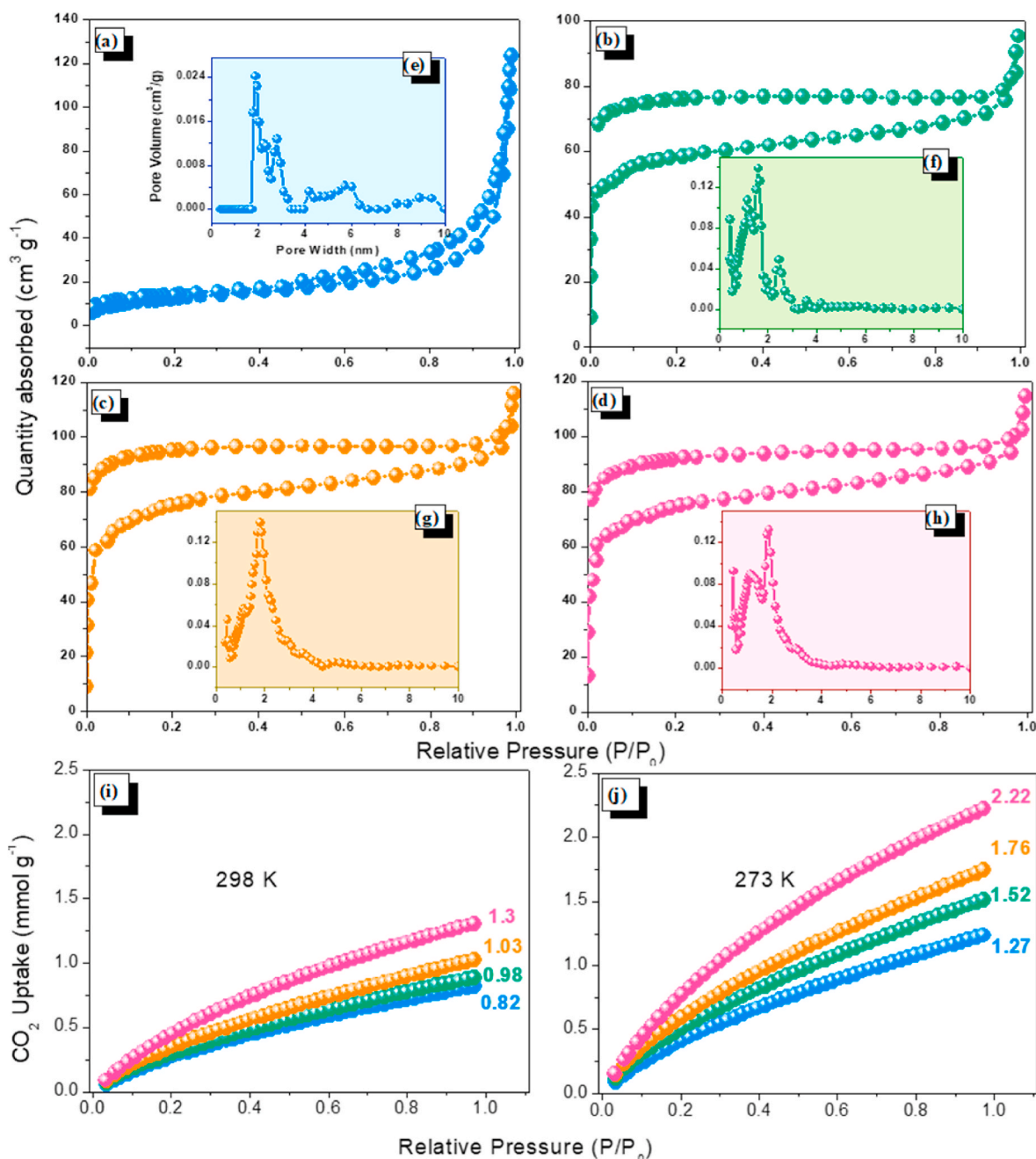

Fig. 2. (A) SEM and (B) TEM of (a1, b1) Py–FC–CMP, (a2, b2) TBN–FC–CMP, (a3, b3) TPE–FC–CMP, and (a4, b4) BP-FC-CMP.

Fig. 3. (a–d) N_2 sorption isotherms and (e–h) PSD curves of (a, e) Py–FC–CMP, (b, f) TBN–FC–CMP, (c, g) TPE–FC–CMP, and (d, h) BP-FC-CMP. (i, j) CO_2 adsorptions of Py–FC–CMP, TBN–FC–CMP, TPE–FC–CMP and BP-FC-CMP measured at (i) 298 and (j) 273 K.

photoelectron spectroscopy (XPS) to estimate the elemental compositions of the AFC-CMPs (Fig. S12). X-ray photoelectron spectroscopy (XPS) was performed to estimate the elemental composition of the AFC-CMPs [Fig. S12]. The XPS spectra revealed three peaks at ca. 286, 420, and 534 eV due to C, N (pyridyl), and O atoms. Moreover, the Fe element in ferrocene moiety featured a peak at a binding energy of 700 eV [65], confirming the integration of the ferrocene unit into the AFC-CMPs networks.

The AFC-CMPs morphologies were examined by using both scanning and transmission electron microscopies [Fig. 2(A) and 2(B)]. The SEM and TEM images of TBN–FC–CMP, TPE–FC–CMP, and BP-FC-CMP revealed the assemblage of nonuniform spherical particles, while those of Py–FC–CMP revealed an assemblage of rodlike shapes [Fig. 2(a1, b1)]. Moreover, the elemental mapping (EDS) was performed from SEM image to identify the chemical composition of the BP-AFC-CMP sample

[Fig. S13]. The EDS mapping demonstrated the existence of C, N, O, and Fe elements that proportionated with the XPS result.

The porous parameters of the AFC-CMPs were checked by employing N_2 adsorption-desorption isotherms analysis that was performed at a temperature of 77 K as shown in [Fig. 3(a-d) and Table 1]. Accordingly, the BET values of Py–FC–CMP, TBN–FC–CMP, TPE–FC–CMP, and BP-FC-CMP were evaluated to be 72, 217, 271, and 341 $m^2 g^{-1}$, respectively. In addition, all BET curves for all samples displayed type I or IV adsorption and desorption isotherms, indicating the presence of mesoporous and microporous structures in AFC-CMPs frameworks. As well, the pore size distribution profiles were estimated depending on the N_2 sorption isotherms of the AFC-CMPs by applying nonlocalized DFT (NLDFT) theory [Fig. 3(e-h) and Table 1]. Consequently, the results of PSD profiles showed that all AFC-CMPs surfaces include micropores with average diameters ranging from 0.40 to 1.90 nm. Additionally, CO_2 capture
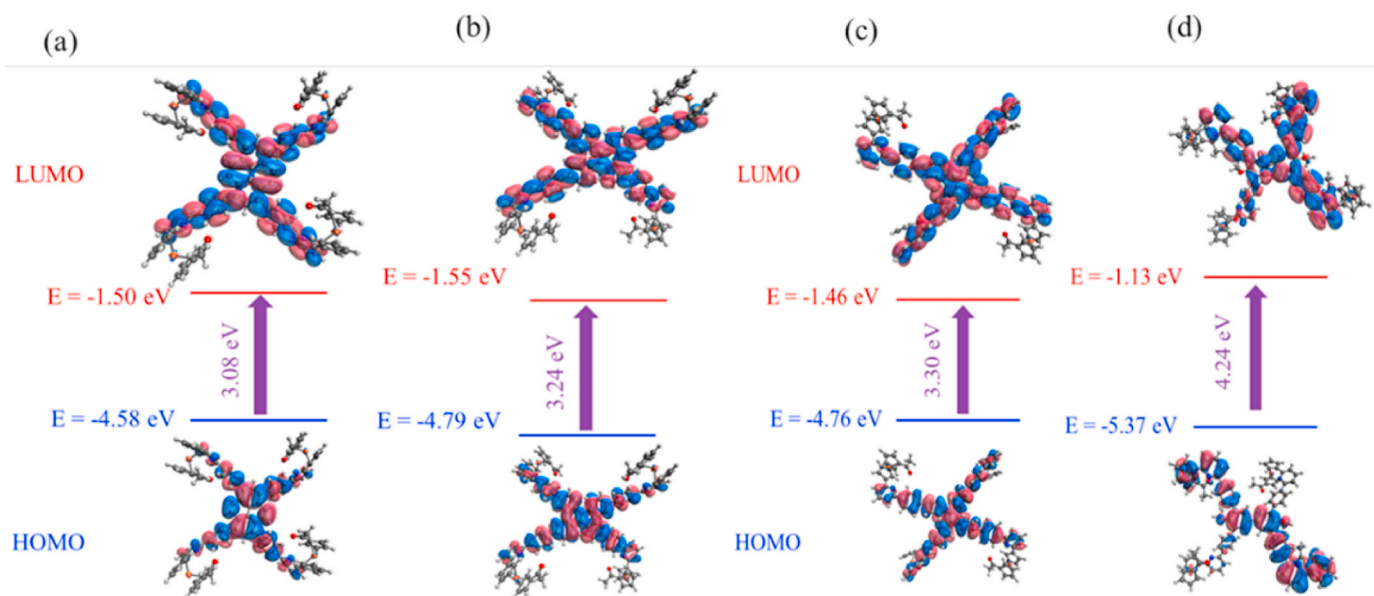
Fig. 4. Energy levels diagrams of (a) Py-FC, (b) TBN-FC, (c) TPE-FC, and (d) BP-FC-CMPs.
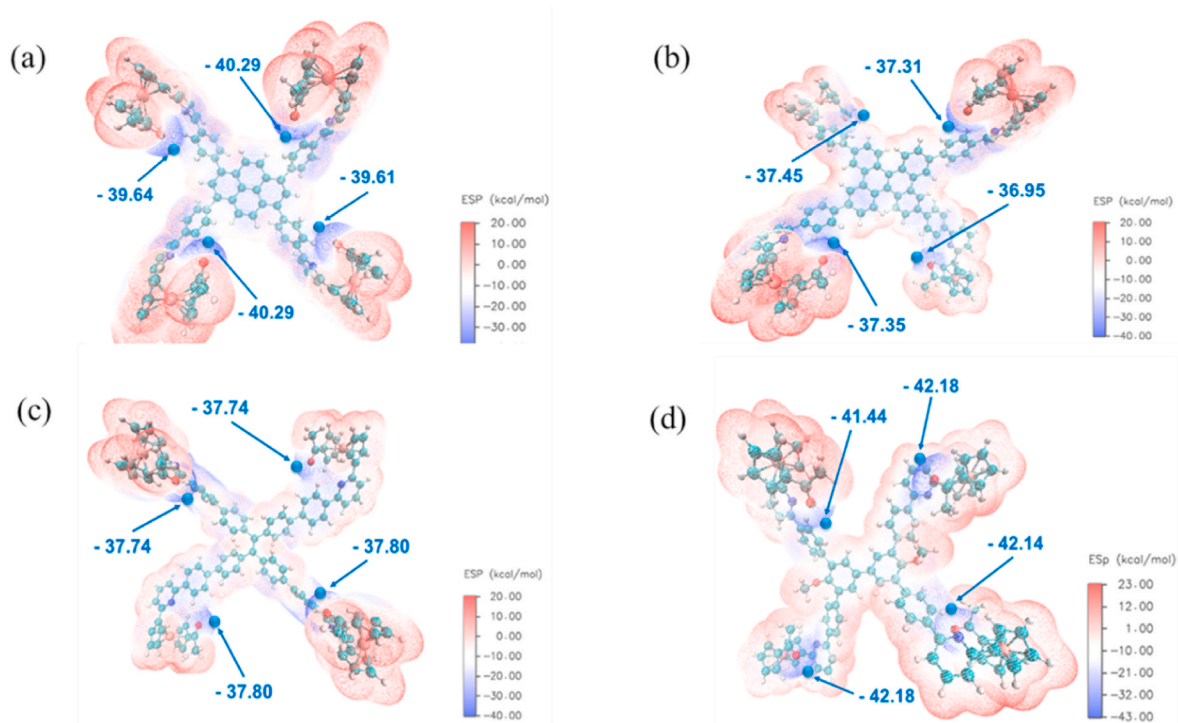

Fig. 5. MESP diagrams of (a) Py–FC–CMP, (b) TBN–FC–CMP, (c) TPE–FC–CMP, and (d) BP-FC-CMP.

measurements of the AFC-CMPs were measured at temperatures of 298, and 273 K at1 bar [Fig. 3(i and j)]. The amount of CO_2 adsorbed by Py–FC–CMP, TBN–FC–CMP, TPE–FC–CMP, and BP-FC-CMP at 298 K was 0.82, 0.98, 1.03, and 1.3 mmol g^{-1}, respectively, whereas, at 273 K, it was 1.27, 1.52, 1.76, and 2.22 mmol g^{-1}, respectively. Notably, BP-FC-CMP offered the highest adsorbed CO_2 ability compared with the other AFC-CMPs, owing to the former having the highest surface area (341 m^2 g^{-1}) that is favorable properties for CO_2 adsorption in porous materials [69–73].

Because the redox and charge storage characteristics of CMPs are influenced by their electronic structures, we used DFT to investigate the electronic structures of our synthesized materials to understand their

electrochemical performance. Here, we employed the basis set 6-31G using the hybrid functional B3LYP (d); to accommodate long-range and noncovalent interactions, we employed the D3BJ dispersion correction. For the ground-state geometries of the monomers, we investigated many conformers and chose the one with the lowest energy. The global minimum was confirmed using the harmonic vibrational frequency. At the same level of theory, the highest occupied molecular orbital (HOMO)–lowest unoccupied molecular orbital (LUMO) energy gaps and the molecule electrostatic potentials were calculated using the optimized geometries. Because the LUMO distribution generally influences a polymer's electrochemical performance significantly, we calculated the frontier molecular orbitals of the monomers AFC, Py-
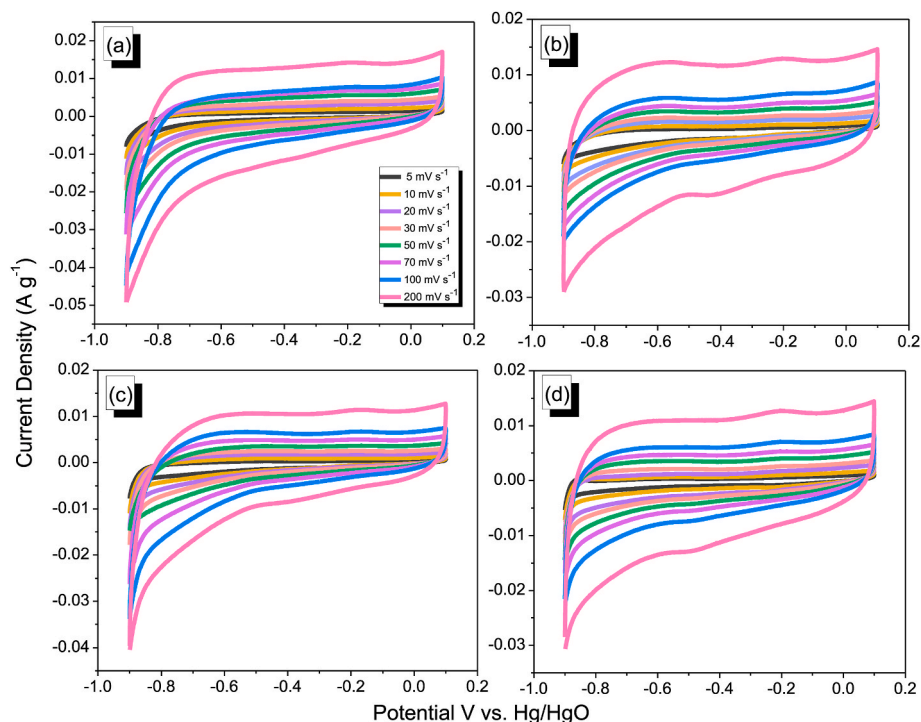
Fig. 6. CV curves of (a) Py-FC, (b) TBN-FC, (c) TPE-FC, and (d) BP-FC-CMPs, recorded at different scan rates.

CHO, TBN-CHO, TPE-CHO, and BP-CHO. For these five monomers, both the HOMOs and LUMOs were strongly delocalized and spanned each whole molecule [Fig. S14]. Fig. 4 displays the HOMOs and LUMOs of the Py–FC–, TBN–FC–, TPE–FC–, and BP-FC-CMPs. The HOMOs and LUMOs in these CMPs were not distributed evenly throughout the molecules. The conjugation did not include the Fc moieties. Fig. 5 and Fig. S15 present the results of molecular electrostatic potential (MESP) analysis of the synthesized monomers and four polymers. The charge density decreased across the redox-active areas in all of the polymers, due to delocalization. In the redox-active sites, however, the O atoms of the acyl groups were more negative in these systems.
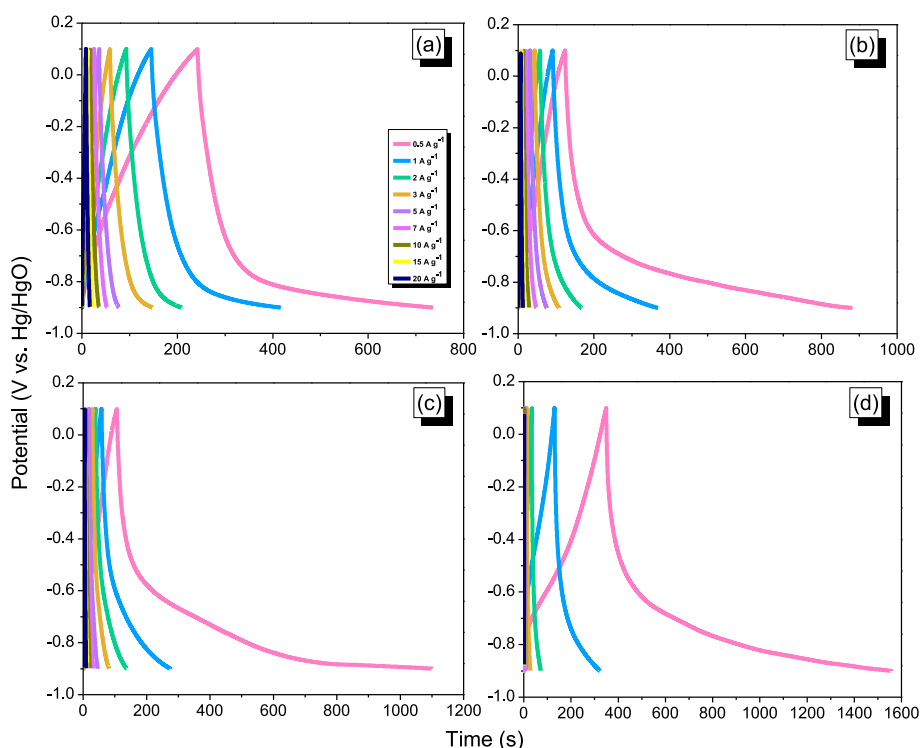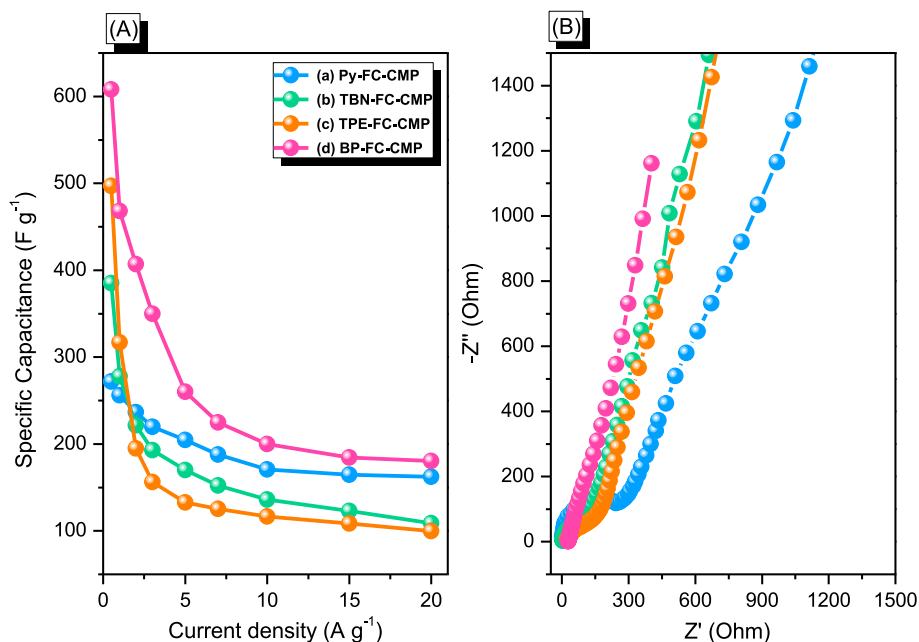

Fig. 7. GCD curves of (a) Py-FC, (b) TBN-FC (c) TPE-FC, and (d) BP-FC-CMPs.
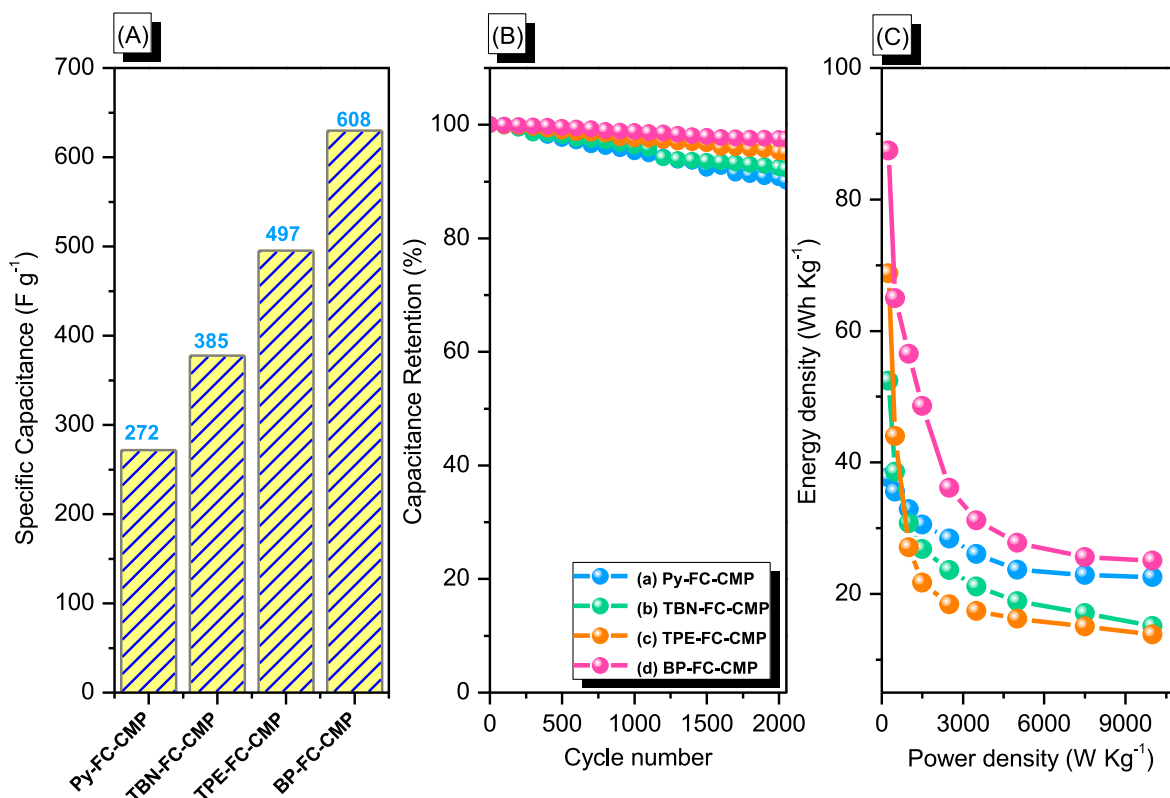
Fig. 8. (A) Specific Capacitance and (B) Electrochemical impedance (Nyquist plots) curves of (a) Py-FC, (b) TBN-FC, (c) TPE-FC, and (d) BP-FC-CMPs examined between 1 and 100 KHz frequencies in 1 M KOH electrolyte.

3.3. Electrochemical evaluation

We used cyclic voltammetry (CV), galvanostatic charge/discharge (GCD) measurements, and electrochemical impedance spectroscopy (EIS) to examine the electrochemical performance of our prepared Fc-based CMPs. We measured the CV curves of Py-FC, TBN-FC, TPE-FC, and BP-FC-CMPs between −0.9 and + 0.1 V at various scan rates [Fig. 6(a)–(d)]. The CV profiles of all of the AFC-CMPs were almost rectangular, with small humps at a lower potential, suggesting EDLC behavior. The humps present in the CV profiles were due to the pseudocapacitance behavior, arising from the combined effects of the heteroatoms (e.g., N atoms) in the pyridine rings and the ferrocene units. In addition, when the scan rate was increased from 5 to 200 mV s^{-1}, the current densities also increased without deteriorating the shapes of the CV profiles, suggesting better rate capabilities, stabilities, and kinetics profiles for all of the CMPs containing Fc moieties. The difference in

Fig. 9. Specific Capacitance (at 0.5 A g^{-1}), (B) Cycling stabilities and (C) Ragone plots of (a) Py-FC, (b) TBN-FC (c) TPE-FC and (d) BP-FC-CMPs.

electrochemical performance mainly come from the configuration of the materials components, i.e., the presence of various types of N and O heteroatoms, surface area, and the existence of micro- and meso-porosity, all of which ensured greater accessibility of the electrolyte to the electrode surface, leading to rapid mass transport, and enhanced electrochemical performance. In addition, the porous structure of our AFC-CMPs frameworks provides diffusion channels and more efficient transport of electrolyte ions, thereby improving the electrochemical performance [74,75].

Furthermore, we recorded the GCD performance of Py–FC–CMP, TBN–FC–CMP, TPE–FC–CMP, and BP-FC-CMP at current densities between 0.5 and 20 A g^{-1} [Fig. 7(a)–(d)]. The GCD profiles of all of the CMPs were almost triangular, with a slight twist during the discharge curve, suggesting the combined effects of EDLC and pseudocapacitance behavior. In addition, during the GCD evaluation, the discharging curves were longer than the charging curves, suggesting that the CMPs possessed good capacitance performance. The discharge curves of BP-FC-CMP were larger than those of Py–FC, TBN–FC, and TPE–FC–CMPs, revealing its higher specific capacitance.

The specific capacitances of all the AFC-CMPs were calculated based on the GCD profiles [Fig. 8(A)]. For Py–FC–CMP, the specific capacitance values were 272, 256, 236, 219, 204, 187, 170, 165 and 162 F g^{-1}, respectively, while they were 385, 278, 221, 192, 170, 152, 136, 123 and 109 F g^{-1}, respectively, for TBN–FC–CMP. Also, TBE–FC–CMP featured capacitance values of 497, 317, 195, 156, 133, 125, 117, 108 and 100 F g^{-1}, respectively. BP-FC-CMP exhibited values of 608, 468, 407, 350, 260, 225, 200, 184 and 180 F g^{-1}, respectively, from 0.5 to 20 A g^{-1}. As a result, Py–FC–CMP showed better rate capability among all the samples. This behavior can be explained by the porous structure in Py–FC–CMP which is dominated by mesoporosity as shown in Fig. 3(e), that allows electrolyte ions to diffuse through the inner active sites at higher current densities, resulting in better rate performance. On the contrary, the porous structure of TBN-FCCMP, TPE–FC–CMP, and BP-FC-CMP samples is dominated by microporosity as shown in Fig. 3 (f–h); which prevents the electrolyte ions to penetrate the inner active sites at high current densities, resulting in larger drop in the electric double layer capacitance and poor specific capacitance at higher current densities [76,77]. To fully understand the influence of the ferrocene unit on the specific capacitance, we next performed electrochemical impedance spectroscopy measurements. The obtained Nyquist plots are shown in [Fig. 8(B)]. The resistance of the BP-FC-CMP was smaller as expected compared to those of Py–FC–CMP, TBN–FC–CMP, and TPE–FC–CMP. This behavior can be attributed to the highest surface area, large pore size, structural integrity, and compatibility of all of the CMPs with ferrocene units [78]. The charge transfer values of Py–FC–CMP, TBN–FC–CMP, TPE–FC–CMP, and BP-FC-CMP were 260, 125, 187, and 81 Ω, respectively. In addition, the presence of a characteristic small semicircle in the higher frequency region suggests that internal charge transfer was moderately low in these electrode materials, implying diffusion-controlled behavior.

More interestingly, among our AFC-CMPs, the capacitance of BP-FC-CMP (608 F g^{-1}) was higher when compared with the other synthesized AFC-CMPs and other previously reported CMPs CMP materials [Fig. 9 (A) and Table S1] due to its higher surface area among all when compared to others which allowed the ease of redox reaction with faster kinetics. Furthermore, the cyclic stability profiles were examined which demonstrated the capacity retention of 90.04, 92.21, 95.11, and 97.47% after long 2000 cycles at a current density of 10 A g^{-1} for Py-FC, TBN-FC, TPE-FC, and BP-FC-CMPs, respectively [Fig. 9(B)]. Moreover, Ragone plots of the AFC-CMPs electrodes were recorded by calculating the values of both energy and power densities according to the equations (S2 and S3). Notably, the BP-FC-CMP electrode featured the highest energy density of 87.45 Wh Kg^{-1}, compared with the other AFC-CMPs (Py–FC–CMP = 37.75 Wh Kg^{-1}, TBN–FC–CMP = 52.43 Wh Kg^{-1} and TPE–FC–CMP = 87.45 Wh Kg^{-1}) operating at a power density of 250 W kg^{-1} [Fig. 9(C)].

4. Conclusions

We have prepared novel AFC-CMPs through aminative cyclizations of a Fc derivative with aryl aldehydes without involving any organic solvents or metal catalysts. The as-prepared Fc-based CMPs appear to be promising electrode materials for energy storage applications, due to the ease and fast kinetics of their redox reactions. Among our materials, the BP-FC-CMP electrode featured the highest energy density (87.45 Wh Kg^{-1}), specific capacitance (608 F g^{-1}), and capacity retention (97.47%). Finally, our results represent the outlines for promising ferrocene-based CMPs towards the higher performance charge energy storage applications.

CRediT authorship contribution statement

Maha Mohamed Samy: Data curation, Writing – original draft. **Santosh U. Sharma:** Data curation, Writing – original draft. **Mohamed Gamal Mohamed:** Data curation, Writing – original draft, Supervision. **Ahmed A.K. Mohammed:** Data curation, Writing – original draft. **Swetha V. Chaganti:** Synthesis the material, Data curation. **Jyh-Tsung Lee:** Supervision. **Shiao-Wei Kuo:** Supervision, Writing – review & editing.

Declaration of competing interest

The authors declare that they have no known competing financial interests or personal relationships that could have appeared to influence the work reported in this paper.

Acknowledgments

Appendix A. Supplementary data

Supplementary data to this article can be found online at https://doi.org/10.1016/j.matchemphys.2022.126177.

References

[1] C. Young, T. Park, J.W. Yi, J. Kim, M.S.A. Hossain, Y.V. Kaneti, Y. Yamauchi, Advanced functional carbons and their hybrid nanoarchitectures towards supercapacitor applications, ChemSusChem 11 (2018) 3546–3558, https://doi.org/10.1002/cssc.201801525.

[2] K. Yu, X. Pan, G. Zhang, X. Liao, X. Zhou, M. Yan, L. Xu, L. Mai, Nanowires in energy storage devices: structures, synthesis, and applications, Adv. Energy Mater. 8 (2018) 1802369, https://doi.org/10.1002/aenm.201802369.

[3] P.G. Bruce, B. Scrosati, J.-M. Tarascon, Nanomaterials for rechargeable lithium batteries, Angew. Chem. Int. Ed. 47 (2008) 2930–2946, https://doi.org/10.1002/anie.200702505.

[4] M.G. Mohamed, M.M. Samy, T.H. Mansoure, C.J. Li, W.J. Li, J.H. Chen, K. Zhang, S.W. Kuo, Microporous carbon and carbon/metal composite materials derived from bio-benzoxazine-linked precursor for CO_2 capture and energy storage applications, Int. J. Mol. Sci. 23 (2022) 347, https://doi.org/10.3390/ijms23010347.

[5] Z. Lin, E. Goikolea, A. Balducci, K. Naoi, P.L. Taberna, M. Salanne, G. Yushin, P. Simon, Materials for supercapacitors: when Li-ion battery power is not enough, mater, Today Off. 21 (2018) 419–436, https://doi.org/10.1016/j.mattod.2018.01.035.

[6] M.G. Mohamed, T.H. Mansoure, M.M. Samy, Y. Takashi, A.A.K. Mohammed, T. Ahamad, S.M. Alshehri, J. Kim, B.M. Matsagar, K.C.W. Wu, S.W. Kuo, Ultrastable conjugated microporous polymers containing benzobisthiadiazole and pyrene building blocks for energy storage applications, Molecules 27 (2022) 2025, https://doi.org/10.3390/molecules27062025.

[7] D. Chen, K. Jiang, T. Huang, G. Shen, Recent advances in fiber supercapacitors: materials, device configurations, and applications, Adv. Mater. 32 (2020) 1901806, https://doi.org/10.1002/adma.201901806.

[8] A.F.M. EL-Mahdy, T.E. Liu, S.W. Kuo, Direct synthesis of nitrogen-doped mesoporous carbons from triazine-functionalized resol for CO_2 uptake and highly

efficient removal of dyes, J. Hazard Mater. 391 (2020) 122163, https://doi.org/10.1016/j.jhazmat.2020.122163.

[9] M.G. Mohamed, S.U. Sharma, N.Y. Liu, T.H. Mansoure, M.M. Samy, S.V. Chaganti, Y.L. Chang, J.T. Lee, S.W. Kuo, Ultrastable covalent triazine organic framework based on anthracene moiety as platform for high-performance carbon dioxide adsorption and supercapacitors, Int. J. Mol. Sci. 23 (2022) 3174, https://doi.org/10.3390/ijms23063174.

[10] M.G. Mohamed, S.U. Sharma, C.H. Yang, M.M. Samy, A.A.K. Mohammed, S. V. Chaganti, J.T. Lee, S.W. Kuo, Anthraquinone-enriched conjugated microporous polymers as organic cathode materials for high-performance lithium-ion batteries, ACS Appl. Energy Mater. 4 (2021) 14628–14639, https://doi.org/10.1021/acsaem.1c03270.

[11] M.G. Mohamed, M.M. Samy, T.H. Mansoure, S.U. Sharma, M.S. Tsai, J.H. Chen, J. T. Lee, S.W. Kuo, Dispersions of 1,3,4-oxadiazole-linked conjugated microporous polymers with carbon nanotubes as a high-performance electrode for supercapacitors, ACS Appl. Energy Mater. 5 (2022) 3677–3688, https://doi.org/10.1021/acsaem.2c00100.

[12] N. Meng, X. Ren, G. Santagiuliana, L. Ventura, H. Zhang, J. Wu, H. Yan, M.J. Reece, E. Bilotti, Ultrahigh β-phase content poly(vinylidene fluoride) with relaxor-like ferroelectricity for high energy density capacitors, Nat. Commun. 10 (2019) 4535, https://doi.org/10.1038/s41467-019-12391-3.

[13] A.F.M. EL-Mahdy, T.C. Yu, M.G. Mohamed, S.W. Kuo, Secondary structures of polypeptide-based diblock copolymers influence the microphase separation of templates for the fabrication of microporous carbons, Macromolecules 54 (2021) 1030–1042, https://doi.org/10.1021/acs.macromol.0c01748.

[14] H. Zhao, J. Wang, Y. Zheng, J. Li, X. Han, G. He, Y. Du, Organic thiocarboxylate electrodes for a room-temperature sodium ion battery delivering an ultrahigh capacity, Angew. Chem. Int. Ed. 56 (2017) 15334–15338, https://doi.org/10.1002/anie.201708960.

[15] A. Eftekhari, B. Fang, Electrochemical hydrogen storage: opportunities for fuel storage, batteries, fuel cells, and supercapacitors, Int. J. Hydrogen Energy 42 (2017) 25143–25165, https://doi.org/10.1016/J.IJHYDENE.2017.08.103.

[16] M.M. Samy, M.G. Mohamed, S.W. Kuo, Pyrene functionalized tetraphenylethylene polybenzoxazine for dispersing single-walled carbon nanotubes and energy storage, Compos. Sci. Technol. 199 (2020) 108360, https://doi.org/10.1016/j.compscitech.2020.108360.

[17] M.M. Samy, M.G. Mohamed, S.W. Kuo, Directly synthesized nitrogen-and-oxygen–doped microporous carbons derived from a bio-derived polybenzoxazine exhibiting high-performance supercapacitance and CO₂ uptake, Eur. Polym. J. 138 (2020) 109954, https://doi.org/10.1016/j.eurpolymj.2020, 109954.

[18] D. Kim, J. Kang, B. Yan, K.D. Seong, Y. Piao, Ambient temperature synthesis of iron-doped porous nickel pyrophosphate nanoparticles with long-term chemical stability for high-performance oxygen evolution reaction catalysis and supercapacitors, ACS Sustain. Chem. Eng. 8 (2020) 2843–2853, https://doi.org/10.1021/acssuschemeng.9b06920.

[19] Y. Wang, W. Li, L. Zhang, X. Zhang, B. Tan, J. Hao, J. Zhang, X. Wang, Q. Hu, X. Lu, Amorphous cobalt hydrogen phosphate nanosheets with remarkable electrochemical performances as advanced electrode for supercapacitors, J. Power Sources 449 (2020) 227487, https://doi.org/10.1016/j.jpowsour.2019.227487.

[20] R. Shi, C. Han, H. Duan, L. Xu, D. Zhou, H. Li, J. Li, F. Kang, B. Li, G. Wang, Redox-active organic sodium anthraquinone-2-sulfonate (AQS) anchored on reduced graphene oxide for high-performance supercapacitors, Adv. Energy Mater. 8 (2018) 1802088. http://hdl.handle.net/10453/133607.

[21] N.L.W. Septiani, Y.V. Kaneti, K.B. Fathoni, J. Wang, Y. Ide, B. Yuliarto, Nugraha, H. K. Dipojono, A.K. Nanjundan, D. Golberg, Y. Bando, Y. Yamauchi, Self-assembly of nickel phosphate-based nanotubes into two-dimensional crumpled sheet-like architectures for high-performance asymmetric supercapacitors, Nano Energy 67 (2020) 104270, https://doi.org/10.1016/j.nanoen.2019.104270.

[22] M. Thommes, K. Kaneko, A.V. Neimark, J.P. Olivier, F.R. Reinoso, J. Rouquerol, K. S.W. Sing, Physisorption of gases, with special reference to the evaluation of surface area and pore size distribution (IUPAC Technical Report), Pure Appl. Chem. 87 (2015) 1051–1069, https://doi.org/10.1515/pac-2014-1117.

[23] J.S.M. Lee, A.I. Cooper, Advances in conjugated microporous polymers, Chem. Rev. 120 (2020) 2171–2214, https://doi.org/10.1021/acs.chemrev.9b00399.

[24] T.X. Wang, H.P. Liang, D.A. Anito, X. Ding, B.H. Han, Emerging applications of porous organic polymers in visible-light photocatalysis, J. Mater. Chem. 8 (2020) 7003–7034, https://doi.org/10.1039/D0TA00364F.

[25] M.G. Mohamed, M.H. Elsayed, A.M. Elewa, A.F.M. EL-Mahdy, C.H. Yang, A. K. Mohammed, H.H. Chou, S.W. Kuo, Pyrene containing conjugated organic microporous polymers for photocatalytic hydrogen evolution from water, Catal. Sci. Technol. 11 (2021) 2229–2241, https://doi.org/10.1039/D0CY02482A.

[26] Y. Sang, G. Chen, J. Huang, Oxygen-rich porous carbons from carbonyl modified hyper-cross-linked polymers for efficient CO₂ capture, J. Polym. Res. 27 (2020) 36, https://doi.org/10.1007/s10965-020-2009-9.

[27] Y. Byun, S.H. Je, S.N. Talapaneni, A. Coskun, Advances in porous organic polymers for efficient water capture, Chem. Eur J. 25 (2019) 10262–10283, https://doi.org/10.1002/chem.201900940.

[28] A.F.M. EL-Mahdy, C. Young, J. Kim, J. You, Y. Yamauchi, S.W. Kuo, Hollow microspherical and microtubular [3+ 3] carbazole-based covalent organic frameworks and their gas and energy storage applications, ACS Appl. Mater. Interfaces 11 (2019) 9343–9354, https://doi.org/10.1021/acsami.8b21867.

[29] Y. Cui, J. Du, Y. Liu, Y. Yu, S. Wang, H. Pang, Z. Liang, J. Yu, Design and synthesis of a multifunctional porous N-rich polymer containing s-triazine and Tröger's base for CO₂ adsorption, catalysis and sensing, Polym. Chem. 9 (2018) 2643–2649, https://doi.org/10.1039/C8PY00177D.

[30] M.G. Kotp, A.F.M. El-Mahdy, T.L. Yang, S.W. Kuo, A pyridinyl-phenanzine conjugated microporous polymer decorated with ultrafine Ag nanoparticles mediates the rapid reduction of nitrophenol Microporous, Mesoporous Mater 331 (2022) 111669, https://doi.org/10.1016/j.micromeso.2021.111669.

[31] M.G. Mohamed, C.C. Lee, A.F.M. EL-Mahdy, J. Lüder, M.H. Yu, Z. Li, Z. Zhu, C. C. Chueh, S.W. Kuo, Exploitation of two-dimensional conjugated covalent organic frameworks based on tetraphenylethylene with bicarbazole and pyrene units and applications in perovskite solar cells, J. Mater. Chem. A 8 (2020) 11448–11459, https://doi.org/10.1039/D0TA02956D.

[32] J.X. Jiang, F. Su, A. Trewin, C.D. Wood, N.L. Campbell, H. Niu, C. Dickinson, A. Y. Ganin, M.J. Rosseinsky, Y.Z. Khimyak, A.I. Cooper, Conjugated microporous poly(aryleneethynylene) networks, Angew. Chem. Int. Ed. 46 (2007) 8574–8578, https://doi.org/10.1002/anie.200701595.

[33] K.I. Aly, M.M. Sayed, M.G. Mohamed, S.W. Kuo, O. Younis, A facile synthetic route and dual function of network luminescent porous polyester and copolyester containing porphyrin moiety for metal ions sensor and dyes adsorption, Microporous Mesoporous Mater. 298 (2020) 110063, https://doi.org/10.1016/j.micromeso.2020.110063.

[34] F. Vilela, K. Zhang, M. Antonietti, Conjugated porous polymers for energy applications, Energy Environ. Sci. 5 (2012) 7819–7832, https://doi.org/10.1039/C2EE22002D.

[35] J. Schmidt, M. Werner, A. Thomas, Conjugated microporous polymer networks via Yamamoto polymerization, Macromolecules 42 (2009) 4426–4429, https://doi.org/10.1021/MA900547.

[36] S. Fischer, A. Schimanowitz, R. Dawson, I. Senkovska, S. Kaskel, A. Thomas, Cationic microporous polymer networks by polymerisation of weakly coordinating cations with CO₂-storage ability, J. Mater. Chem. 2 (2014) 11825–11829, https://doi.org/10.1039/C4TA02022G.

[37] M.M. Samy, M.G. Mohamed, T.H. Mansoure, T.S. Meng, M.A.R. Khan, C.C. Liaw, S. W. Kuo, Solid state chemical transformations through ring-opening polymerization of ferrocene-based conjugated microporous polymers in host–guest complexes with benzoxazine-linked cyclodextrin, J. Taiwan Inst. Chem. Eng. 132 (2022) 104110, https://doi.org/10.1016/j.jtice.2021.10.010.

[38] S.B. Ren, P.X. Li, A. Stephenson, L.J. Chen, M.E. Briggs, R. Clowes, A. Alahmed, K. K. Li, W.P. Jia, D.M. Han, 1,3-Diyne-linked conjugated microporous polymer for selective CO₂ capture, Ind. Eng. Chem. Res. 57 (2018) 9254–9260, https://doi.org/10.1021/acs.iecr.8b01401.

[39] M.G. Mohamed, T.H. Mansoure, Y. Takashi, M.M. Samy, T. Chen, S.W. Kuo, Ultrastable porous organic/inorganic polymers based on polyhedral Oligomeric silsesquioxane (POSS) hybrids exhibiting high performance for thermal property and energy storage, Microporous Mesoporous Mater. 328 (2021) 111505, https://doi.org/10.1016/j.micromeso.2021.111505.

[40] M.G. Mohamed, T.C. Chen, S.W. Kuo, Solid-state chemical transformations to enhance gas capture in benzoxazine-linked conjugated microporous polymers, Macromolecules 54 (2021) 5866–5877, https://doi.org/10.1021/acs.macromol.1c00736.

[41] M.M. Samy, M.G. Mohamed, A.F.M. El-Mahdy, T.H. Mansoure, K.C.W. Wu, S. W. Kuo, High-performance supercapacitor electrodes prepared from dispersions of tetrabenzonaphthalene-based conjugated microporous polymers and carbon nanotubes, ACS Appl. Mater. Interfaces 13 (2021) 51906–51916, https://doi.org/10.1021/acsami.1c05720.

[42] G.Y. Li, L. Qin, C. Yao, Y.H. Xu, Controlled synthesis of conjugated Polycarbazole polymers via structure tuning for gas storage and separation applications, Sci. Rep. 7 (2017) 15394, https://doi.org/10.1038/s41598-017-10372-4.

[43] M.G. Mohamed, M.Y. Tsai, C.F. Wang, C.F. Huang, M. Danko, L. Dai, T. Chen, S. W. Kuo, Multifunctional polyhedral oligomeric silsesquioxane (POSS) based hybrid porous materials for CO₂ uptake and iodine adsorption, Polymers 13 (2021) 221, https://doi.org/10.3390/polym13020221.

[44] M.G. Mohamed, M.M.M. Ahmed, W.T. Du, S.W. Kuo, Meso/microporous carbons from conjugated hyper-crosslinked polymers based on tetraphenylethene for high-performance CO₂ capture and supercapacitor, Molecules 26 (2021) 738, https://doi.org/10.3390/molecules26030738.

[45] B. Bonillo, R.S. Sprick, A.I. Cooper, Tuning photophysical properties in conjugated microporous polymers by comonomer doping strategies, Chem. Mater. 28 (2016) 3469–3480, https://doi.org/10.1021/acs.chemmater.6b01195.

[46] M.G. Mohamed, E.C.A. Jr, B.M. Matsagar, J. Na, Y. Yamauchi, K.C.W. Wu, S. W. Kuo, Construction hierarchically mesoporous/microporous materials based on block copolymer and covalent organic framework, J. Taiwan Inst. Chem. Eng. 112 (2020) 180–192, https://doi.org/10.1016/j.jtice.2020.06.013.

[47] M.G. Mohamed, N.Y. Liu, A.F.M. EL-Mahdy, S.W. Kuo, Ultrastable luminescent hybrid microporous polymers based on polyhedral Oligomeric silsesquioxane for CO₂ uptake and metal ion sensing, Microporous Mesoporous Mater. 311 (2021) 110695, https://doi.org/10.1016/j.micromeso.2020.110695.

[48] C. Zhang, Y. Qao, P.X. Xiong, W.Y. Ma, P.X. Bai, X. Wang, Q. Li, J. Zhao, Y.F. Xu, Y. Chen, J.H. Zeng, F. Wang, Y.H. Xu, J.X. Jiang, Conjugated microporous polymers with tunable electronic structure for high-performance potassium-ion batteries, ACS Nano 13 (2019) 745–754, https://doi.org/10.1021/acsnano.8b08046.

[49] A.M. Elewa, A.F.M. EL-Mahdy, M.H. Elsayed, M.G. Mohamed, S.W. Kuo, H. H. Chou, Sulfur-doped triazine-conjugated microporous polymers for achieving the robust visible-light-driven hydrogen evolution, Chem. Eng. J. 421 (2021) 129825, https://doi.org/10.1016/j.cej.2021.129825.

[50] P.Y. Ju, S.J. Wu, Q. Su, X.D. Li, Z.Q. Liu, G.H. Li, Q.L. Wu, Salen-porphyrin-based conjugated microporous polymer supported Pd nanoparticles: highly efficient heterogeneous catalysts for aqueous C-C coupling reactions, J. Mater. Chem. 7 (2019) 2660–2666, https://doi.org/10.1039/C8TA11330K.

[51] N. Keller, M. Calik, D. Sharapa, H.R. Soni, P.M. Zehetmaier, S. Rager, F. Auras, A. C. Jakowetz, A.T. Goerling, C.T. Bein, Enforcing extended porphyrin J-aggregate stacking in covalent organic frameworks, J. Am. Chem. Soc. 140 (2018) 16544–16552, https://doi.org/10.1021/jacs.8b08088.

[52] Y.Y. Dai, W.J. Li, Z.X. Chen, X.G. Zhu, J.L. Liu, R.Y. Zhao, D.S. Wright, A. Noori, M. F. Mousavi, C. Zhang, An air-stable electrochromic conjugated microporous polymer as an emerging electrode material for hybrid energy storage systems, J. Mater. Chem. 7 (2019) 16397–16405, https://doi.org/10.1039/C9TA03001H.

[53] M.G. Mohamed, W.C. Chen, A.F.M. El-Mahdy, S.W. Kuo, Porous organic/inorganic polymers based on double-decker silsesquioxane for high-performance energy storage, J. Polym. Res. 28 (2021) 219, https://doi.org/10.1007/s10965-021-02579-x.

[54] Z. Meng, K. Sato, T. Sutegana, K. Oyaizu, C.L. Ho, J. Xiang, Y.H. Feng, Y.H. Lo, H. Nishide, W.Y. Wong, Metallopolyyne polymers with ferrocenyl pendant ligands as cathode-active materials for organic battery application, J. Organomet. Chem. 812 (2016) 51–55, https://doi.org/10.1016/j.jorganchem.2015.11.019.

[55] G. Cong, Y.C. Zhou, Z.J. Li, Y.C. Lu, A Highly concentrated catholyte enabled by a low-melting-point ferrocene derivative, ACS Energy Lett. 2 (2017) 869–875, https://doi.org/10.1021/acsenergylett.7b00115.

[56] C. Zhang, Y.M. Qian, Y. Ding, L. Zhang, X. Guo, Y. Zhao, G. Yu, Biredox eutectic electrolytes derived from organic redox-active molecules: high-energy storage systems, Angew. Chem. Int. Ed. 58 (2019) 7045–7050, https://doi.org/10.1002/anie.201902433.

[57] Q.Y. Zhang, X.L. Cui, L. Zhang, S.Z. Luo, H. Wang, Y. Wu, Metal-and reagent-free highly selective anodic cross-coupling reaction of phenols, Angew. Chem. Int. Ed. 54 (2015) 5210–5213, https://doi.org/10.1002/anie.201500070.

[58] H. Mandai, K. Fujii, H. Yasuhara, K. Abe, K. Mitsudo, T. Korenaga, S. Suga, Enantioselective acyl transfer catalysis by a combination of common catalytic motifs and electrostatic interactions, Nat. Commun. 7 (2016) 11297, https://doi.org/10.1038/ncomms11297.

[59] T.L. Choi, K.H. Lee, W.J. Joo, S. Lee, T.W. Lee, M.Y. Chae, Synthesis and nonvolatile memory behavior of redox-active conjugated polymer-containing ferrocene, J. Am. Chem. Soc. 129 (2007) 9842–9843, https://doi.org/10.1021/ja0717459.

[60] J. Xiang, X.L. Li, Y. Ma, Q. Zhao, C.L. Ho, W.Y. Wong, Efficient flash memory devices based on non-conjugated ferrocene-containing copolymers, J. Mater. Chem. C 6 (2018) 11348–11355, https://doi.org/10.1039/C8TC03140A.

[61] J. Tan, H. Li, X.X. Hu, R. Abdullah, S. Xie, L. Zhang, M. Zhao, Q. Luo, Y. Li, Z. Sun, Q. Yuan, W. Tan, Size-tunable assemblies based on ferrocene-containing DNA polymers for spatially uniform penetration, Inside Chem. 5 (2019) 1775–1792, https://doi.org/10.1016/j.chempr.2019.05.024.

[62] Q. Dong, Z. Meng, C.L. Ho, H. Guo, W. Yang, I. Manners, L. Xu, W.Y. Wong, Molecular approach to magnetic metallic nanostructures from metallopolymer precursors, Chem. Soc. Rev. 47 (2018) 4934–4953, https://doi.org/10.1039/C7CS00599G.

[63] Y. Wang, J. Tao, S. Xiong, P. Lu, J. Tang, J. He, M.U. Javaid, C. Pan, G. Yu, Ferrocene-based porous organic polymers for high-affinity iodine capture, Chem. Eng. J. 380 (2020) 122420, https://doi.org/10.1016/j.cej.2019.122420.

[64] L. Ma, Y. Liu, Y. Liu, S. Jiang, P. Li, Y. Hao, P. Shao, A. Yin, X. Feng, B. Wang, Ferrocene-linkage-facilitated charge separation in conjugated microporous polymers, Angew. Chem. Int. Ed. 58 (2019) 4221–4226, https://doi.org/10.1002/anie.201813598.

[65] Z. Tan, H. Su, Y. Guo, H. Liu, B. Liao, A.M. Amin, Q. Liu, Ferrocene-based conjugated microporous polymers derived from Yamamoto coupling for gas storage and dye removal, Polymers 12 (2020) 719, https://doi.org/10.3390/polym12030719.

[66] Z. Wei, D. Wang, Y. Liu, X. Guo, Y. Zhu, Z. Meng, Ferrocene-based hyperbranched polymers: a synthetic strategy for shape control and applications as electroactive materials and precursor-derived magnetic ceramics, J. Mater. Chem. C 8 (2020), https://doi.org/10.1039/D0TC01380C, 10774–80.

[67] A.M. Khattak, H. Sin, Z.A. Ghaz, X. He, B. Liang, N.A. Khan, H.R. Alanagh, A. Iqbal, L. Li, Z. Tang, Controllable fabrication of redox-active conjugated microporous polymers on reduced graphene oxide for high performance faradaic energy storage, J. Mater. Chem. 6 (2018) 18827, https://doi.org/10.1039/C8TA07913G.

[68] Z. Cheng, L. Wang, Y. He, X. Chen, X. Wu, H. Xu, Y. Liao, M. Zhu, Rapid metal-free synthesis of pyridyl-functionalized conjugated microporous polymers for visible-light driven water splitting, Polym. Chem. 11 (2020) 3393, https://doi.org/10.1039/D0PY00249F.

[69] H. Wang, Z. Cheng, Y. Liao, J. Li, J. Weber, A. Thomas, C.F.J. Faul, Conjugated microporous polycarbazole networks as precursors for nitrogen-enriched microporous carbons for CO_2 storage and electrochemical capacitors, Chem. Mater. 29 (2017) 4885–4893, https://doi.org/10.1021/acs.chemmater.7b00857.

[70] W. Wang, M. Zhou, D. Yuan, Carbon dioxide capture in amorphous porous organic polymers, J. Mater. Chem. 5 (2017) 1334–1347, https://doi.org/10.1039/C6TA09234A.

[71] M.G. Mohamed, A.F.M. EL-Mahdy, Y. Takashi, S.W. Kuo, Ultrastable conductive microporous covalent triazine frameworks based on pyrene moieties provide high-performance CO_2 uptake and supercapacitance, New J. Chem. 44 (2020) 8241–8253, https://doi.org/10.1039/D0NJ01292K.

[72] M.G. Mohamed, A.F.M. EL-Mahdy, M.G. Kotp, S.W. Kuo, Advances in porous organic polymers: syntheses, structures, and diverse applications, Mater. Adv. 3 (2022) 707–733, https://doi.org/10.1039/D1MA00771H.

[73] M.G. Mohamed, A.F.M. EL-Mahdy, M.M.M. Ahmed, S.W. Kuo, Direct synthesis of microporous bicarbazole based covalent triazine frameworks for high performance energy storage and carbon dioxide uptake, ChemPlusChem. 84 (2019) 1767–1774, https://doi.org/10.1002/cplu.201900635.

[74] S. Kondrat, C.R. Pérez, V. Presser, Y. Gogotsi, A.A. Kornyshev, Effect of pore size and its dispersity on the energy storage in nanoporous supercapacitors, Energy Environ. Sci. 5 (2012) 6474–6479, https://doi.org/10.1039/C2EE03092F.

[75] S.Y. Park, C.W. Kang, S.M. Lee, H.J. Kim, Y.J. Ko, J. Choi, S.U. Son, Nanoparticulate conjugated microporous polymer with post-modified benzils for enhanced pseudocapacitor performance, Chem. Eur. J. 26 (2020) 12343–12348, https://doi.org/10.1002/chem.202002311.

[76] S. Bandyopadhyay, C. Singh, P. Jash, M.W. Hussain, A. Paul, A. Patra, Redox-active, pyrene-based pristine porous organic polymers for efficient energy storage with exceptional cyclic stability, Chem. Commun. 54 (2018) 6796–6799, https://doi.org/10.1039/C8CC02477D.

[77] M. Arunkumar, A. Paul, Importance of electrode preparation methodologies in supercapacitor applications, ACS Omega 2 (2017) 8039–8050, https://doi.org/10.1021/acsomega.7b01275.

[78] R. Takahashi, S. Sato, T. Sodesawa, H. Nishida, Effect of pore size on the liquid-phase pore diffusion of nickel nitrate, Phys. Chem. Chem. Phys. 4 (2002) 3800–3805, https://doi.org/10.1039/B202024F.